Article

A Robust Adaptive Unscented Kalman Filter for Floating Doppler Wind-LiDAR Motion Correction

Andreu Salcedo-Bosch [1], Francesc Rocadenbosch [1,2,*] and Joaquim Sospedra [3]

[1] CommSensLab-UPC, Unidad de Excelencia María de Maeztu, Department of Signal Theory and Communications, Universitat Politècnica de Catalunya (UPC), E-08034 Barcelona, Spain; andreu.salcedo@upc.edu
[2] Institut d'Estudis Espacials de Catalunya (IEEC), Universitat Politècnica de Catalunya, E-08034 Barcelona, Spain
[3] Laboratori d'Enginyeria Maritima, Universitat Politècnica de Catalunya, E-08034 Barcelona, Spain; joaquim.sospedra@upc.edu
* Correspondence: francesc.rocadenbosch@upc.edu

Abstract: This study presents a new method for correcting the six degrees of freedom motion-induced error in ZephIR 300 floating Doppler Wind-LiDAR-derived data, based on a Robust Adaptive Unscented Kalman Filter. The filter takes advantage of the known floating Doppler Wind-LiDAR (FDWL) dynamics, a velocity–azimuth display algorithm, and a wind model describing the LiDAR-retrieved wind vector without motion influence. The filter estimates the corrected wind vector by adapting itself to different atmospheric and motion scenarios, and by estimating the covariance matrices of related noise processes. The measured turbulence intensity by the FDWL (with and without correction) was compared against a reference fixed LiDAR over a 25-day period at "El Pont del Petroli", Barcelona. After correction, the apparent motion-induced turbulence was greatly reduced, and the statistical indicators showed overall improvement. Thus, the Mean Difference improved from −1.70% (uncorrected) to 0.36% (corrected), the Root Mean Square Error (RMSE) improved from 2.01% to 0.86%, and coefficient of determination improved from 0.85 to 0.93.

Keywords: floating Doppler Wind LiDAR; apparent turbulence; motion compensation; adaptive filtering; Kalman Filter; Unscented Kalman Filter; six degrees of freedom

1. Introduction

In recent decades, the wind energy (WE) industry has shown a rising interest in deploying offshore wind farms, due to the higher and more homogeneous winds that can be found in open-sea environments [1,2]. Important investments have been made in Europe, in terms of deploying and operating offshore wind farms [3]. The high deployment and operation cost of these facilities has motivated the industry to search for cost reduction solutions [4,5]. One of the main concerns is to obtain trustable data to assess the viability of future offshore wind farm projects [6]. Traditionally, meteorological masts (metmast) have been used for this purpose [7]. As offshore wind farms are deployed further offshore into deeper waters [8], metmasts are not a feasible solution. FDWLs are a cost-effective alternative to metmasts, which can assess the wind resource in a more flexible way [5].

Multiple validation campaigns have shown the robustness and reliability of horizontal wind speed (HWS) and wind direction (WD) FDWL measurements at the ten-minute level [9–13]. However, FDWLs measure an increased turbulence intensity (TI), in contrast to fixed Doppler Wind LiDARs (DWLs), due to wave-induced motion [14]. TI is defined as the ratio between the standard deviation of the HWS to the mean HWS. Wave-induced motion adds variance to FDWL HWS measurements, resulting in higher TI [15].

TI is a relevant parameter in wind farm design and operation [16]. For instance, erroneous TI could lead to over-design of the wind turbines, causing extra costs. Therefore,

there is a need to compensate for the effect of wave-induced motion on FDWL measurements [17,18]. Both the rotational motion (roll, pitch, and yaw) and translational motion (surge, sway, and heave) of the LiDAR induce errors in the retrieved HWS and WD [19,20]. The latter is of lesser concern because WD errors can easily be corrected by means of a reference compass installed on the buoy [21]. Multiple approaches have been presented for reduction of the motion-induced error in FDWL measurements. In the study published by Gutiérrez-Antuñano et al. [21], a dual approach was proposed, in which an averaging window technique was combined with mechanical compensation by means of a cardanic frame; however, the cardanic frame increases the hardware costs of the device, and is not able to compensate for translational motion. Moreover, the averaging window technique is not able to compensate for motion frequencies higher than the LiDAR sampling rate. Gutiérrez-Antuñano et al. [13] presented a statistical solution based on a FDWL system simulator. The simulator considered basic motion parameters (lidar roll and pitch angular amplitude and period), as well as reference HWS and WD, to simulate the motion-induced error on TI measurements. This method showed overall good correction, but the results differed under distinct wind and motion scenarios. Kelberlau et al. [20] proposed a signal processing algorithm that took into account all 6 degrees of freedom (DoF) of LiDAR motion, to correct for the motion-induced error at a line-of-sight (LoS) level. Although the algorithm was able to eliminate the motion-induced TI error under virtually all motion conditions, it requires access to the LiDAR LoS internal measurements, which is undisclosed information for most of the commercial continuous-wave LiDARs. Last, but not least, state-of-the-art motion-correction algorithms rely on off-line data post-processing, which is disadvantageous.

In this study, we aim to correct the motion-induced error on wind measurements by a floating continuous-wave conical-scanning DWL without accessing LoS information. We rely on the fact that successively measured wind observations tend to be correlated and that past measurements provide a priori information on the wind vector at the current estimation time [22,23]. Moreover, the LiDAR measurement process and the wave-induced 6-DoF LiDAR motion can be accurately modelled. In this scenario, the Kalman Filter (KF) is considered to be a promising candidate for tackling this problem. The KF is used to estimate discrete time-series, which are governed by linear differential operators [24]. It can estimate the hidden variables of a dynamic system from observations over time.

In non-linear systems, as in our case, the plain KF is not adequate to solve the problem. Instead, upgrades of the KF, such as the Extended KF (EKF) or the Unscented KF (UKF) [25], are used. In this study, we present a Robust Adaptive Unscented Kalman Filter (RAUKF) based on the FDWL model proposed by Kelberlau et al. [20], to estimate the LiDAR-retrieved wind vector without motion influence. We rely on the FDWL geometrical model and the Velocity–Azimuth Display (VAD) LiDAR wind-retrieval algorithm [26].

Filter performance is assessed using experimental data from the "El Pont del Petroli" (PdP) campaign, in which a proof-of-concept FDWL buoy was compared, with reference to a fixed LiDAR [21]. This allowed us to compare the motion-corrected FDWL TI to the fixed-LiDAR reference TI.

The remainder of this paper is structured as follows: Section 2 presents the instrumental setup and models the FDWL (motion and VAD algorithm counterparts) and the wind process, Section 2.6 formulates the motion-compensation problem using the state-space representation of the physical model, and Section 2.7 summarizes the RAUKF method. Section 3 presents the PdP campaign and motion-correction results. Section 4 provides our concluding remarks.

2. Materials and Methods

2.1. Instrumental Setup

In 2013, the Neptune project "proof-of-concept" LiDAR buoy validation campaign at PdP took place between May 24th and June 31st [21,27]. During the campaign, a proof-of-concept floating DWL buoy was compared against a fixed LiDAR, denoted "FDWL"

and "fixed LiDAR", respectively, in the following. Both the FDWL and the fixed LiDAR were ZephIR^{TM} 300 LiDARs. The fixed LiDAR was set up in stand-still configuration on PdP pier, as the reference device. The FDWL and the fixed LiDAR were located 50 m apart (see Figure 1). Both LiDARs were calibrated onshore, 1 m apart and over a period of 3 h, to ensure identical measurements on a 1 s and 10 min time basis. PdP is located on the coastline of Badalona (Barcelona, Spain), in the Barcelona metropolitan area. The experiment location surroundings are defined by an urban topology of low-height buildings (up to 20 m), which follow the coastline in the west and north cardinal directions, while the rest is defined by a sea-type topology.

Figure 1. PdP campaign location map and experimental setup.

The ZephIR 300 is a continuous-wave focused Doppler LiDAR manufactured by Zephir Ltd., United Kingdom (today ZX LiDARs^{TM}), which is prepared for offshore operation [28]. The device can measure the wind at user-defined heights between 10 m to 200 m, in steps of 1 m [29]. The LiDAR uses the VAD algorithm to retrieve the wind vector by measuring 50 LoSs at equally spaced azimuth angles (7.2-deg azimuth step between LoSs) along a conical scan of 30-deg aperture width from zenith. The ZephIR 300 can reach up to 1 scan/s when there is no LiDAR re-focusing required or CPU dead-time internal processes [29].

The FDWL was mounted on a proof-of-concept 3 m diameter buoy, designed as a prototype for offshore LiDAR operations. The buoy design was optimized for LiDAR measurements, as well as for tracking wave-induced motion on the device. The LiDAR was placed on a cardanic frame, aimed to keep the instrument still and to reduce the impact of buoy motion. The buoy was equipped with additional sensors, to measure different wind and sea parameters. Specifically, it hosted two MicroStrain 3DM-GX3-45 inertial measurement units (IMU), which combined a high-precision GPS antenna, an accelerometer, and a gyro. The first IMU (i.e., the LiDAR IMU) was located under the LiDAR bottom, and the second IMU (i.e., the buoy IMU) was located on the buoy structure bottom (see Figure 2), being able to measure the buoy and LiDAR attitude. During the campaign, different LiDAR measurement configurations were tested.
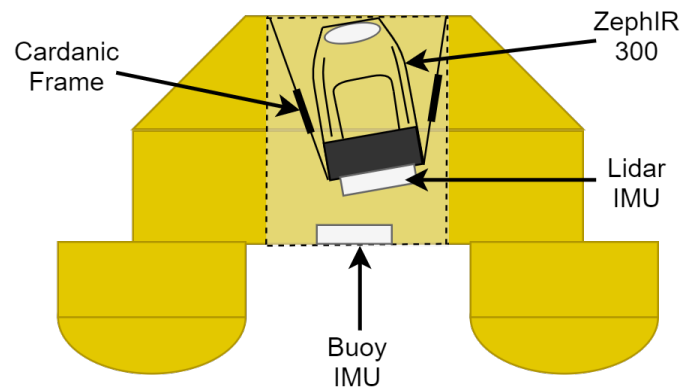
Figure 2. Instrumentation scheme of the FDWL proof-of-concept buoy used in PdP campaign.

2.2. Basic Theoretical Definitions

The wind vector, $\boldsymbol{U}$, is defined as a three-component vector formed by the *HWS*, *WD* (clockwise from north), and vertical wind speed (*VWS*), as

$$\boldsymbol{U} = \begin{bmatrix} HWS \\ WD \\ VWS \end{bmatrix}. \tag{1}$$

In WE, a standard sampling period of 10 min was used. The mean wind conditions at this resolution were obtained by simply averaging the high-resolution (1 s) wind-vector components into a 10 min period. Thus, the mean *HWS* was computed as

$$\overline{HWS} = \frac{1}{N} \sum_{n=1}^{N} HWS_n, \tag{2}$$

where HWS_n is the high-resolution *HWS* measurement and $N = 600$ is the number of 1 s measurements in one minute.

We are also interested in the *HWS* variations, with respect to the mean *HWS*. This variability was measured by means of the *TI*, which is defined as

$$TI = \frac{\sigma_{HWS}}{\overline{HWS}}, \tag{3}$$

where σ_{HWS} is the 10 min *HWS* standard deviation. The standard deviation is defined as

$$\sigma_{HWS} = \sqrt{\frac{1}{N-1} \sum_{n=1}^{N} (HWS_n - \overline{HWS})}. \tag{4}$$

2.3. The Estimation Viewpoint

The KF relies on two steps to estimate the hidden state-vector of the physical system under study: The prediction step and the innovation step [24].

The *prediction step* is defined by two equations, which are formulated in state-space notation as

$$\boldsymbol{x}_{k|k-1} = f(\boldsymbol{x}_{k-1|k-1}) + \boldsymbol{v}_k, \tag{5}$$

$$\boldsymbol{z}_{k|k-1} = h(\boldsymbol{x}_{k|k-1}) + \boldsymbol{n}_k. \tag{6}$$

The first equation is the *prediction equation*, in which $\boldsymbol{x}_{k|k-1}$ is the hidden state-vector to be estimated, based on the previous state-vector estimate, $\boldsymbol{x}_{k-1|k-1}$. Sub-indices $n|m$ denote estimation at the discrete time instant n, conditioned to all available information up to time m. Here, $\boldsymbol{x}_{k|k-1}$ is the motion-free wind vector to be estimated, based on previous

wind-vector estimations. $f(\cdot)$ is the state-transition function predicting the state-vector at discrete time k, $\boldsymbol{x}_{k|k-1}$, given previous knowledge of the state-vector, $\boldsymbol{x}_{k-1|k-1}$; that is, $f(\cdot)$ describes the stochastic wind model (to be found) that predicts the measured wind vector at the next time step from the wind vector at the previous one. $\boldsymbol{v}_k$ is the process noise. The temporal resolution is the scan period (1 s approximately, see Section 2.4).

The second equation is the *measurement equation*, which estimates the present-time measurement, $\boldsymbol{z}_{k|k-1}$, given the *a priori* state-vector, $\boldsymbol{x}_{k|k-1}$, and motion information (to be further developed in Section 2.6), through the measurement function $h(\cdot)$. In other words, the measurement function models the FDWL motion dynamics and estimates the expected motion-corrupted wind measurements, based on the *a priori* state-vector and IMU motion information vector $\boldsymbol{M}$ (to be defined in Section 2.6). $\boldsymbol{n}_k$ is the measurement noise.

On the other hand, the *innovation step* allows for the assimilation of the present-time measurement information into the a priori state-vector estimate through a projection gain (the so-called Kalman gain). Formally,

$$\hat{\boldsymbol{x}}_{k|k} = \boldsymbol{x}_{k|k-1} + \boldsymbol{K}_k(\boldsymbol{z}_k - \boldsymbol{z}_{k|k-1}), \tag{7}$$

where $\boldsymbol{z}_k$ is the wind-vector measurement and $\boldsymbol{K}_k$ is the Kalman gain matrix. The latter relates the measurement estimation error, $\Delta\boldsymbol{z} = \boldsymbol{z}_{k|k} - \boldsymbol{z}_{k|k-1}$, to the a priori state-vector estimation error, $\Delta\boldsymbol{x} = \boldsymbol{x}_{k|k} - \boldsymbol{x}_{k|k-1}$.

To implement the UKF, both the state-transition wind model $f(.)$ and FDWL motion-dynamics measurement function $h(.)$ must be found. This is tackled in the following section.

2.4. The Measurement Model: FDWL Motion

The wind vector is retrieved from the Doppler wind projection along the LoSs in the conical scan pattern by means of the VAD algorithm (see Section 2.4.3). In real operating conditions of the FDWL, sea-induced motion disturbs the conical scan, such that the pointing direction and measured radial velocities become affected by rotational and translational motion. In the motion-correction study by Kelberlau et al. [20], a complete geometrical description of the problem is thoroughly given. Next, we summarize and adapt information from this reference which are relevant to derive the measurement function $h(.)$ shown in Equation (6) above.

To describe the FDWL system, we first define the right-handed Cartesian XYZ "moving-body" coordinate system of the buoy and the north–east–down right-handed Cartesian NED "fixed" global frame of reference (see Figure 3). The latter is the inertial frame of reference in which the wind vector and FDWL motion are defined. Without external influence, the X, Y, and Z axes of the moving-body coordinate system are aligned with the north, east, and vertically down vectors of the fixed NED frame of reference. Wind, waves, and external forces cause translational motion in the N, E, and D directions (surge, sway, and heave, respectively), and rotational motion along the N, E, and D axes (roll, pitch, and yaw, respectively). We define $\hat{x}$, $\hat{y}$, and $\hat{z}$ as unit vectors aligned with the X, Y, and Z axes of the moving-body coordinate system. On the other hand, $\hat{n}$, $\hat{e}$, and $\hat{d}$ are defined as the unit vectors aligned with the north, east, and vertically down axes of the global NED frame of reference. $\tilde{h}$ is defined as the LiDAR beam direction before the prism deflection. The vector $\hat{h}$ is defined as the opposite vector to $\hat{z}$. The LoSs are measured in a cone of ϕ_0-deg width from $\hat{h}$. Finally, we define θ_0 as the LiDAR initial scan phase (i.e., the azimuth angle of the LiDAR pointing direction at the first LoS; denoted $\hat{r}_1$), with respect to $\hat{x}$ in the XY plane. During a scan, the LiDAR pointing direction $\hat{r}$ ranges from $\theta = -\theta_0$ to $\theta = -\theta_0 + 360 \times 1s$, with a fixed step $\Delta\theta$ between consecutive LoSs in a scan, which are denoted by $\hat{r}_n$ and $\hat{r}_{n+1}$, where n is the LoS number.

Figure 3. Schematic of the motion geometry of the FDWL buoy. (**a**) The moving-body coordinate system (red arrows) and the fixed coordinate system (blue arrows). (**b**) The LiDAR scanning cone and LiDAR pointing direction (green arrows) in relation to the XYZ coordinate system.

2.4.1. Rotational Motion

The rotational model (to be formulated as function $h_{rot}(\cdot)$ in Section 2.6) computes the "true" LiDAR pointing direction vectors by means of a series of geometrical operations. Rotational motion affects the LiDAR pointing direction in each LoS, $\hat{r}_n, n = 1, \dots, 50$. A series of chained vector rotations (refer to [20], Equations (5)–(12)) are needed to *re-encounter $\hat{r}$ in the NED reference frame* (in the following, $\hat{r}$ will be used as shorthand notation for the vector set $\hat{r}_n, n = 1, \dots, 50$). This is derived next:

The Euler rotation matrix is used to express $\hat{x}$, $\hat{y}$, and $\hat{z}$ in the NED frame of reference given roll, pitch, and yaw values ([20], Equations (5)–(7)). The unitary vector $\hat{h}$ in the direction of the laser beam, before it is deflected by the LiDAR prism, is computed as ([20], Equation (8)):

$$\hat{h} = -\hat{z}. \tag{8}$$

$\hat{e}_{\theta_0}$, which denotes the vector in the direction of LiDAR heading in the N-E plane (i.e., the azimuth angle of $\hat{r}_1$), is obtained by rotating $\hat{x}$ along $\hat{h}$ by θ deg, as:

$$\hat{e}_{\theta_1} = R(\hat{h}, \theta) \cdot \hat{x}, \tag{9}$$

where $R(\hat{h}, \theta)$ is the rotation matrix about $\hat{h}$ θ degrees ([20], Equation (9)). Then, auxiliary vector $\hat{e}_{\theta_{270}}$, defined as the unit vector perpendicular to $\hat{e}_{\theta_0}$ in the N-E plane, is encountered as ([20], Equation (10)):

$$\hat{e}_{\theta_{270}} = \hat{h} \times \hat{e}_{\theta_0}. \tag{10}$$

Finally, the first LiDAR pointing direction $\hat{r}_1$ can be expressed in the NED frame of reference by rotating $\hat{h}$ by ϕ_0 deg along $\hat{e}_{\theta_{270}}$, as:

$$\hat{r}_1 = R(\hat{e}_{\theta_{270}}, \phi_0) \cdot \hat{h}. \tag{11}$$

The remaining LiDAR pointing directions in a scan, $\hat{r}_n, n = 2, \ldots, 50$ are obtained by changing the scan angle θ_0 into θ_{n-1}, with n as above.

2.4.2. Translational Motion

The translational model (formulated as function $h_{trans}(\cdot)$ in Section 2.6) computes the set of 50 LiDAR-measured, LoS radial velocities during a scan, $\boldsymbol{v}_{LoS}$. Translational motion also influences the measured LoS velocities. To study its effects, we need to account for all the velocity components at the position of the LiDAR scanning prism (origin of the scanning cone, O' in Figure 3). First, we define $\vec{d}$ as the distance vector between the origin of the NED coordinate system (O in Figure 3) and that of the scanning cone in the NED frame of reference (O' in Figure 3). The velocity experienced at measurement location O', $\vec{v_{lidar}}$, becomes influenced by both the translational velocities experienced by the LiDAR and rigid-body motion caused by the angular velocities. This composite effect can be expressed as ([20], Equation (14))

$$\vec{v_{lidar}} = \hat{n}v_n + \hat{e}v_e + \hat{d}v_d + (\hat{n}\omega_n) \times \vec{d} + (\hat{e}\omega_e) \times \vec{d} + (\hat{d}\omega_d) \times \vec{d}, \tag{12}$$

where v_n, v_e, and v_d are surge, sway, and heave motions, respectively, and ω_n, ω_e and ω_d are roll, pitch, and yaw angular velocities, respectively.

Finally, the translational velocity contribution into a LoS ([20], Equation (15)) is the projection of $\vec{v_{lidar}}$ onto $\hat{r}$ ([20], Equation (15)):

$$v_{LoS} = \hat{r} \cdot \vec{v_{lidar}}. \tag{13}$$

The radial velocity measured by the LiDAR along a LoS is encountered as the difference between the wind-vector projection over $\hat{r}$ and v_{LoS}, as:

$$v_r = \vec{U} \cdot \hat{r} - v_{LoS}. \tag{14}$$

2.4.3. VAD Algorithm

The VAD model (formulated as $h_{VAD}(\cdot)$ in Section 2.6) retrieves the wind vector $\boldsymbol{U}$ from the measured LoS velocities, $\boldsymbol{v}_{LoS}$. Assuming a uniform wind field, the measured radial wind, as a function of the azimuth LiDAR scan angle, takes the form of a cosine wave [26]. The VAD algorithm uses the least-squares method (LSQ) to fit a sinusoidal function to the measured radial velocities in the conical scan, v_r, at LoS azimuth angles ϕ. Formally,

$$v_r(\phi) = |A \cos (\phi - B) + C|, \tag{15}$$

where A, B, and C are the LSQ solving variables, which yield the wind-vector information as:

$$\begin{aligned} HWS &= A / \sin (\phi), \\ WD &= B \pm 180 \, deg, \\ VWS &= C / \cos (\phi). \end{aligned} \tag{16}$$

The sign ambiguity in the WD is due to the ZephIR 300 homodyne LiDAR detection, i.e., the LiDAR can only measure unsigned Doppler frequency shifts, which leads to 180-deg ambiguity in the WD retrieved by the VAD algorithm [26]. This ambiguity is resolved by means of the wind vane installed on the buoy.

2.5. State-Transition Model

2.5.1. Wind Model

The LiDAR-retrieved wind vector is a non-stationary stochastic process dependent on the atmospheric conditions [30]. For instance, the wind field gusty nature causes high wind speed increments during short time periods [16]. Although physically rooted, advanced turbulent models describing the spectral tensor for atmospheric surface-layer

turbulence [22] provide a refined solution, their application is hampered by their complexity and demand for computational resources. Instead, we propose a straightforward and oversimplified approach, in which the wind process is modelled as a random-walk (RW) stochastic process, in a similar fashion as what was used for the initial scan-phase model. It is formulated as:

$$\boldsymbol{U}_k = \boldsymbol{U}_{k-1} + \boldsymbol{\epsilon}_k, \tag{17}$$

where $\boldsymbol{\epsilon}_k$ is a random variable with zero-mean Gaussian distribution, $N(0, \sigma)$.

Figure 4 compares the HWS time-series estimated from the RW model (Equation (17)) to that measured by the fixed LiDAR. Figure 4a) demonstrates a similar dynamic range and process variability between both time-series, during most of the time. This is corroborated in Figure 4b), in terms of their associated Power Spectral Densities (PSD). Both PSDs were virtually coincident in the first spectral lobe (10 Hz cut off, -15 dB), indicating that RW modelling is a promising candidate for our estimation purposes. Discrepancies above 10 Hz were responsible for partial time-series tracking around sample nos. 150–200 in Figure 4a).
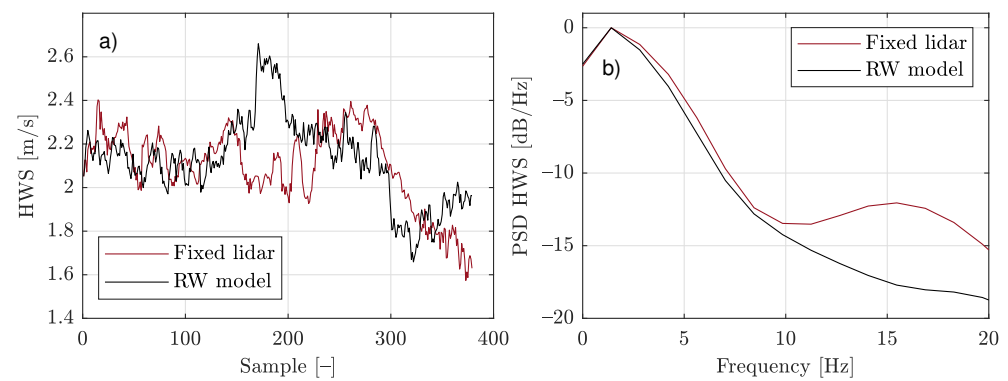
Figure 4. Comparison between the HWS RW model presented in Section 2.5.1 and experimental data: (**a**) Temporal series; and (**b**) PSD.

2.5.2. Initial Scan-Phase Model

The LiDAR initial scan phase, θ_0, has great influence on the measurement error and, therefore, is of key importance for LiDAR motion correction [13]. However, θ_0 is an *undisclosed* parameter from the manufacturer's side, which needs to be estimated. In the motion-correction study by Gutiérrez-Antuñano et al. [13], θ_0 is considered a random variable with uniform probability density from 0 to 360 deg. Based on this assumption, the LiDAR initial scan-phase process is modelled as a RW process, as:

$$\theta_{0,k} = \theta_{0,k-1} + \epsilon_k, \tag{18}$$

where ϵ_k is a uniform random variable in $[0, 360)$ deg.

2.6. State-Space Formulation of the Problem

Once the measurement (Section 2.4) and state-transition *models* (Section 2.5) have been formulated, we aim to derive associated measurement and state-transition *functions* $h(.)$ and $f(.)$, respectively, in accordance with the state-space formulation presented in Section 2.3.

State-transition function $f(.)$.- To derive the state-transition function, first we considered the "clean" (i.e., motion-free) wind vector, $\boldsymbol{U}_k$, which is to be estimated from the motion-corrupted wind vector $\boldsymbol{U}_k^{FDWL}$ from the FDWL. The state-vector to be estimated, $\boldsymbol{x_k}$, is formed by the clean wind vector at time k, $\boldsymbol{U}_k$, and the LiDAR initial scan phase at that discrete time, $\theta_{0,k}$. This is formulated as

$$\boldsymbol{x}_k = \begin{bmatrix} \boldsymbol{U}_k^T & \theta_{0,k} \end{bmatrix}^T, \tag{19}$$

which using Equation (1), can be expanded to

$$\boldsymbol{x}_k = \begin{bmatrix} HWS_k & WD_k & VWS_k & \theta_{0,k} \end{bmatrix}^T. \tag{20}$$

By inserting the state-vector Equation (20) above, along with the RW models for the wind and initial scan-phase processes (Equations (17) and (18), respectively) into prediction Equation (5), we obtain

$$\boldsymbol{x}_{k|k-1} = \boldsymbol{I} \cdot \boldsymbol{x}_{k-1|k-1} + \boldsymbol{v}_k, \tag{21}$$

where $\boldsymbol{I}$ is the identity matrix. This enables us to identify state-transition function $f(\cdot)$, as:

$$f(\boldsymbol{x}_{k-1|k-1}) = \boldsymbol{I} \cdot \boldsymbol{x}_{k-1|k-1}. \tag{22}$$

In Equation (22) above, the state-vector is a 4-component vector, estimated at each successive LiDAR scan (i.e., with approximately 1 s temporal resolution). Recall that sub-indices $n|m$ refer to estimation at discrete time n, based on past information up to discrete time m.

Measurement function $h(.)$—The measurement equation (Equation (6)) predicts the *motion-corrupted* wind-vector $\boldsymbol{z}_{k|k-1}$ measured by the FDWL (i.e., the observation vector) from the estimated state-vector, $\boldsymbol{x}_{k|k-1}$. The observation vector is written as

$$\boldsymbol{z}_k = \boldsymbol{U}_k^{FDWL} = [HWS_{FDWL}, WD_{FDWL}, VWS_{FDWL}]^T, \tag{23}$$

where HWS_{FDWL}, WD_{FDWL}, and VWS_{FDWL} are the FDWL measurements of HWS, WD, and VWS, respectively. $\boldsymbol{z}_k$ is a 3-component vector computed at each successive time scan.

As the measurement function $h(\cdot)$ is time variant depending on the attitude motion of the LiDAR, we define the motion block-vector $\boldsymbol{M}_k$ describing the 6-DoF motion of the FDWL during a scan as:

$$\boldsymbol{M}_k = [\boldsymbol{R}_k, \boldsymbol{P}_k, \boldsymbol{Y}_k, \boldsymbol{v}_{\boldsymbol{x}k}, \boldsymbol{v}_{\boldsymbol{y}k}, \boldsymbol{v}_{\boldsymbol{d}k}], \tag{24}$$

where $\boldsymbol{R}_k, \boldsymbol{P}_k, \boldsymbol{Y}_k, \boldsymbol{v}_{\boldsymbol{x}k}, \boldsymbol{v}_{\boldsymbol{y}k}$, and $\boldsymbol{v}_{\boldsymbol{d}k}$ are the roll, pitch, yaw, surge, sway, and heave time-series measured by the IMU at 10 Hz temporal resolution and interpolated at 50 Hz. Numerically, the block-vector $\boldsymbol{M}$ is a 50×6 matrix, where each row is a LoS attitude measurement, and each column is an attitude parameter.

Assuming uniform wind flow during the LiDAR scan at time k, the motion-corrupted FDWL observations in a scan can be described by a set of three successive operations (Section 2.4, and refer to Figure 5):

(i) retrieval of the motion-corrupted instantaneous LoS set, $\hat{\boldsymbol{r}}$;
(ii) estimation of the associated LoS velocities, $\boldsymbol{v}_{LoS}$; and
(iii) VAD retrieval of the motion-corrupted observation wind vector, $\boldsymbol{z}_{k|k-1}$;

where $\hat{\boldsymbol{r}}$ denotes the block-vector $[\hat{r}_1, \hat{r}_2, ..., \hat{r}_n]$, $n = 1, \cdots, 50$, and each component represents the nth LoS unit vector (Figure 3).
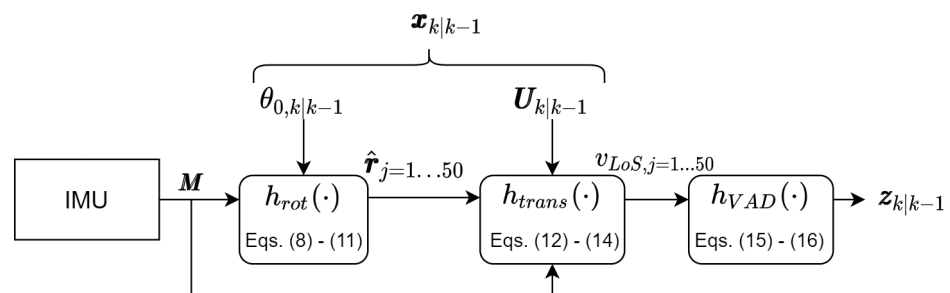

Figure 5. Block diagram depicting the measurement function $h(.)$, as a chain process in which rotation, translation, and VAD retrieval are modelled as elementary functions. Equation numbers inside each block refer to pertinent equations in the text.

Figure 5 block diagram depicts the filter measurement function $h(\cdot)$ as a chain calculus process:

First, at each discrete time k, the 50 motion-corrupted LoSs during the scan ($[\hat{r}_1, \hat{r}_2, ..., \hat{r}_n]$, $n = 1, \cdots, 50$) are computed by means of the geometrical operations presented in Section 2.4.1 (Equations (9)–(12)). This set of operations is denoted $h_{rot}(\cdot)$ in Figure 5. The function $h_{rot}(\cdot)$ computes the block-vector $\hat{\boldsymbol{r}} = [\hat{r}_1, \hat{r}_2, ..., \hat{r}_{50}]$ in the global NED frame of reference based on roll, pitch, and yaw instantaneous angles from attitude vector $\boldsymbol{M}_k$ and predicted initial phase $\theta_{0,k|k-1}$ from the state-vector, $\boldsymbol{x}_{k|k-1}$. Therefore, the block-vector $\hat{\boldsymbol{r}}$ can be written as

$$\hat{\boldsymbol{r}} = h_{rot}(\boldsymbol{x}_{k|k-1}, \boldsymbol{M}_k). \tag{25}$$

Second, the motion-corrupted LoS velocities at time k, $\boldsymbol{v}_{LoS,k}$, are calculated through the set of operations described in Section 2.4.2 (Equations (12) and (13)), and denoted $h_{trans}(\cdot)$ in Figure 5. Function $h_{trans}(\cdot)$ computes this set of velocities given the predicted wind vector, $\boldsymbol{U}_{k|k-1}$, the estimated LoS directions from the previous block, $\hat{\boldsymbol{r}}$, and by considering the influence of LiDAR translational and rigid-body motion information, through Equation (14) and Section 2.4.2, given $\boldsymbol{M}_k$. Then, $\boldsymbol{v}_{LoS,k}$ is obtained as

$$\boldsymbol{v}_{LoS,k} = h_{trans}(\boldsymbol{x}_{k|k-1}, \boldsymbol{M}, \hat{\boldsymbol{r}}). \tag{26}$$

Third, the motion-corrupted VAD-retrieved wind vector $\boldsymbol{z}_{k|k-1}$ is determined from the 50-LoS set of velocities, $\boldsymbol{v}_{LoS,k}$, by means of the least-squares VAD algorithm presented in Section 2.4.3 (Equations (15) and (16)). The VAD algorithm is denoted by $h_{VAD}(\cdot)$ in Figure 5. Hence,

$$\boldsymbol{z}_{k|k-1} = h_{VAD}(\boldsymbol{v}_{LoS,k}). \tag{27}$$

This chain calculus to compute measurement function $h(\cdot)$ can be formulated as the composition of $h_{rot}(\cdot)$, $h_{trans}(\cdot)$, and $h_{VAD}(\cdot)$ functions (through the so-called "chain rule"), as:

$$h(\cdot) = h_{VAD}(\cdot) \circ h_{trans}(\cdot) \circ h_{rot}(\cdot). \tag{28}$$

The time-variant observation model Equation (6) can be formulated as

$$\boldsymbol{z}_{k|k-1} = h(\boldsymbol{x}_{k|k-1}, \boldsymbol{M}) + \boldsymbol{n}_k. \tag{29}$$

2.7. Estimation of State- and Observation-Noise Covariance Matrices

To ensure convergent, unbiased estimates, the UKF must have *a priori* knowledge of both the process noise, $\boldsymbol{v}_k$, and measurement noise, $\boldsymbol{n}_k$. These are zero-mean, additive white Gaussian noise processes with covariances, $\boldsymbol{Q}_k$ and $\boldsymbol{R}_k$, respectively, which must be found. The process-noise covariance matrix, $\boldsymbol{Q}_k$, is defined as

$$\boldsymbol{Q}_k = E[\boldsymbol{v}_k \boldsymbol{v}_k^T]. \tag{30}$$

Likewise, the measurement-noise covariance is defined as

$$\boldsymbol{R}_k = E[\boldsymbol{n}_k \boldsymbol{n}_k^T]. \tag{31}$$

As the measurement function $h(.)$ is time variant with the LiDAR motion vector $\boldsymbol{M}$, so is the measurement noise. Additionally, the wind statistical moments are not stationary, and the noise covariance matrices are difficult to accurately describe. Instead, we propose the adaptive estimation of these matrices based on statistical physical inference [31–33]. In this study, the Robust Adaptive UKF (RAUKF) [34] is chosen, due to its low computational requirements, fast convergence, and overall good performance to adaptively estimate the noise covariances. Moreover, the RAUKF uses a fault-detection mechanism to detect filter failure due to inaccurate estimation of the noise covariance matrices. When a fault is detected, $\boldsymbol{Q}$ and $\boldsymbol{R}$ are adjusted (see Appendix B for details).

In contrast to Equation (30), the RAUKF does not estimate Q as the ensemble average of $v_k v_k^T$ [35,36]. A more straightforward approach is to estimate the matrix Q_k instantaneously (i.e., at each discrete time k), using the approximation $E[v_k v_k^T]$, and to balance it with previous estimates. As a further refinement, the RAUKF dynamically adjusts $\hat{Q}_k$ by blending present and past estimates of the covariance matrix through a forgetting factor, λ, as:

$$\hat{Q}_k = (1 - \lambda)\hat{Q}_{k-1} + \lambda v_k v_k^T. \tag{32}$$

The RAUKF uses similar procedure as for $\hat{Q}_k$, to compute the instantaneous estimations of R_k through a forgetting factor δ, as:

$$\hat{R}_k = (1 - \delta)\hat{R}_{k-1} + \delta n_k n_k^T. \tag{33}$$

A similar memory-fading procedure has been used in the radar application of the filter for atmospheric boundary layer height estimation [37]. In practice, factors in the range 0.1–0.2 provided convergent, unbiased results, as shown in Section 3.

2.8. Filter Initialization

The UKF initial space vector takes the form

$$\hat{x}_0 = [U_0^{proxy}, \theta_{0,0}]^T, \tag{34}$$

where U_0^{proxy} is the "proxy" wind time-series and $\theta_{0,0}$ is initial scan phase, θ_0, at time $k = 0$.

To initialize the filter, a 10 min length, moving-average time-series [21] of the first 1 s-resolution wind measurements (the so-called "proxy" time-series, U_k^{proxy}) is computed. The window length chosen is the wave period over the 10 min series, which is estimated by means of the *L-dB* method [38] (other wave-period estimation methods in the literature [39,40] yielded virtually identical results). The wind component of the state-vector is initialized by retaining the first-time sample of the proxy wind, U_k^{proxy}. The initial scan-phase component of the state-vector is initialized with a random value between 0 and 360 deg, as dictated by the assumption of the *a priori* unknown uniform phase distribution.

The state-noise covariance matrix is linked to RW process noise v_k (Equation (5)). For simplicity, this matrix is assumed to be diagonal. At time $k = 0$, this matrix is written as

$$Q_0 = diag\left(\begin{bmatrix} \sigma_{HWS}^2 & \sigma_{WD}^2 & \sigma_{VWS}^2 & \sigma_{\theta_0'}^2 \end{bmatrix}\right), \tag{35}$$

where each component represents a variance.

As a RW process is characterized at each discrete time by incremental/detrimental random steps away from the previous value of the variable, σ_{HWS}^2, σ_{WD}^2, and σ_{VWS}^2 are estimated as the variance of difference between consecutive samples. For example, σ_{HWS}^2 is calculated from U^{proxy} as

$$\sigma_{HWS}^2 = E[(HWS_k^{proxy} - HWS_{k-1}^{proxy})^2], \tag{36}$$

where $E(.)$ is the expectancy operator (in practice, a 10 min window average). Process noise θ_0 is initialized with the noise variance of a uniform distribution from 0 to 360 deg as

$$\sigma_{\theta_0}^2 = \frac{(b-a)^2}{12} = \frac{360^2}{12}, \tag{37}$$

where $a = 0$ and $b = 360$ deg are the lower and upper limits of the uniform distribution, respectively.

The measurement-noise covariance matrix at initial time, $k = 0$, is formulated as

$$R_0 = diag\left(\begin{bmatrix} \sigma_{R,HWS}^2 & \sigma_{R,WD}^2 & \sigma_{R,VWS}^2 \end{bmatrix}\right), \tag{38}$$

where the subscript R is a remainder of covariance matrix $\boldsymbol{R}_k$ and $\sigma_{R,i}$, $i = HWS, WD, VWS$ is the estimated measurement-noise standard deviation for each of the variables. We used $\sigma_{R,HWS} = 0.05$ m/s, $\sigma_{R,WD} = 50$ deg, and $\sigma_{R,VWS} = 0.025$ m/s for the experimental data of Section 3. These measurement-noise standard deviations were roughly estimated from the 10 min proxy wind time-series, $\boldsymbol{U}_k^{proxy}$, used to initialize the filter. These values were deliberately low, to ensure the smooth start-up of the filter, hence preventing divergence.

Finally, the *a priori* error covariance matrix, $\hat{\boldsymbol{P}}_0^{xx}$, is initialized as

$$\boldsymbol{P}_0^- = \boldsymbol{Q}_0, \tag{39}$$

which indicates that the user's expected *a priori* error during initialization is comparable to the state-noise "nervousness" of the filter, $\boldsymbol{Q}_0$.

3. Results

The motion-compensation algorithm was tested on the PdP experimental campaign by comparing the FDWL with reference to the fixed LiDAR. This is discussed in the following:

3.1. Data Set

The data set used for validation of the motion-correction algorithm comprised data from 6 to 30 June of 2013, with both LiDARs measuring at a fixed height of 100 m; specifically, (i) wind-LiDAR data from the FDWL, (ii) FDWL internal status parameters, and (iii) 6-DoF motion measurements by two IMUs, one on the LiDAR instrument ("lidar IMU" in what follows) and another on the buoy ("buoy IMU"), were used.

Lidar internal status parameters were available, to assess the LiDAR status as well as to ensure the quality of the VAD-retrieved wind-vector measurements. These parameters include the spatial variation (SV), backscatter, and other system parameters. The SV parameter is a LiDAR internal parameter representing the turbulence intensity of the variation degree of the radial wind speeds (LoS) within the circle of scan of the LiDAR [21]. The SV can be understood as a goodness-of-fit parameter of the VAD algorithm which is used to retrieve the wind vector at a given height [26,41]. By experiment, Gutiérrez-Antuñano et al. [21] showed strong correlation between the wind TI and the SV values measured by a fixed ZephIR 300 LiDAR at 100 m in height (SV = 0.02 was approximately related to TI = 5% and SV = 0.1 to TI = 30% therein). The backscatter coefficient is an internal dimensionless parameter indicative of the intensity of the backscattered light return. By experiment, a backscatter threshold of 0.1 is reported in [42] to distinguish between normal and low signal LiDAR returns.

Regarding the IMU data used for motion compensation, each of the IMUs was used for a different purpose: On one hand, the LiDAR IMU was used to measure rotational motion, as the LiDAR was mounted on the cardanic frame in such a way that its rotation center coincided with the LiDAR scan cone apex (location of the scanning prism; point O in Figure 3). On the other hand, the buoy IMU was used to measure translational motion.

3.2. Data Filtering

Lidar-measured data from both the fixed and FDWLs required outlier removal, which encompassed 999X values (a label for system measurement error), too-high wind speed, and rain-flagged data.

The ZephIR 300 LiDAR has a wind measurement range of 1–80 m/s [43]. In high-motion scenarios, wind measurements by the FDWL exhibited high variances as compared to the mean HWS. Ten-minute time-series with a HWS mean lower than 2.5 m/s were removed, to ensure reliable instantaneous HWS measurements [13]. Complex-terrain effects also cause non-negligible effects on the wind flow variability, which may well invalidate the assumption of uniform wind flow during the LiDAR scan [44]. Thus, metropolitan buildings along the coastline cause high spatial variability on the wind field [45], which demonstrates as a non-uniform wind vector along the LiDAR scanning cone. On the other hand, winds blowing from sea to land exhibit higher spatial homogeneity, which leads

to more reliable LiDAR measurements. Following Section 3.1, 1-s data with SV greater than 0.2, which were indicative of spatially non-homogeneous winds, were filtered out. Similarly, data with associated backscatter coefficients smaller than a threshold of 0.02, which is indicative of LiDAR measurements with very low signal return, were rejected.

3.3. Campaign Overview

During the measurement period (6–30 June 2013), the surface layer was dominated by local thermal winds hardly rising above 15 m/s at 100 m in height [21]. The observed HWS in this period ranged from 1 m/s to 15 m/s, with three predominant WDs: North East (NE), North West (NW) and South (S); see Figure 6.
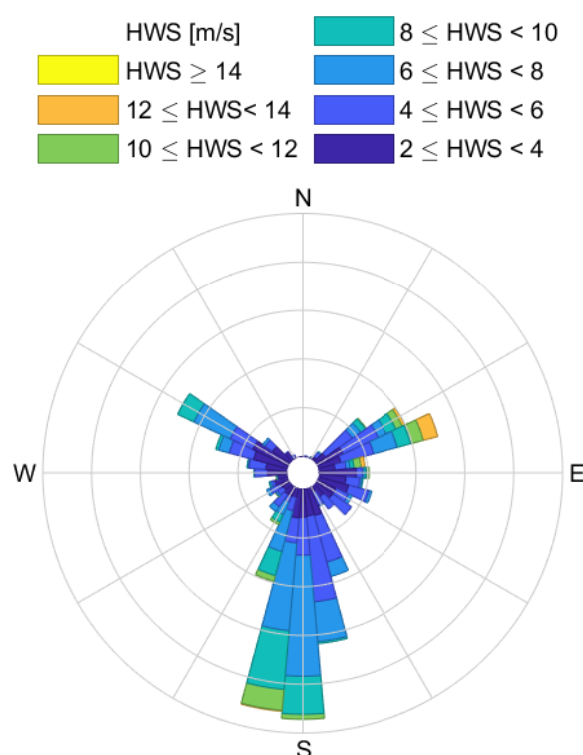
Figure 6. Wind rose representing the HWS and WD (after data filtering), measured during the PdP campaign, by the reference LiDAR (10 min) from June 6 to June 30 of 2013 (1875 records).

During the night, the wind was light, coming predominantly from the urban area (NW), showing low HWS values with high turbulence and spatial variability. During the day, the atmosphere was dominated by winds coming from the sea towards land (S and NE), with higher HWS and lower turbulence.

Both the fixed- and floating-lidar 10 min WD time-series showed unexpected high noise (roughly about ±5-deg uncertainty in Figure 7). This phenomenon is called "granularity" herein, and was caused by a LiDAR flaw. This issue was solved in a later manufacturing series of the instrument [10].
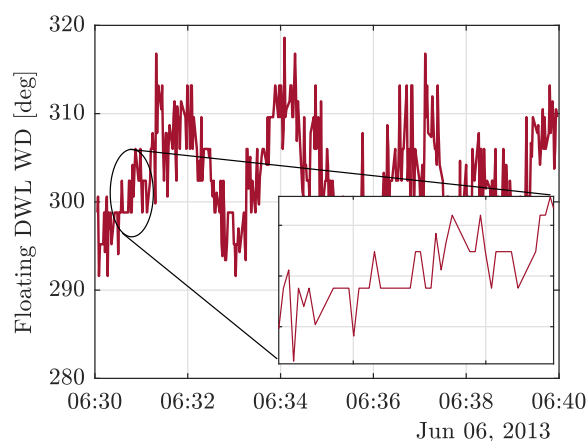
Figure 7. WD time-series measured by the FDWL at 100 m height, showing the so-called "granularity" effect.

3.4. UKF Results

Low/High-turbulence scenario analysis.—The filter was applied to the campaign data set described in Section 3.3. The filter converged in most cases, achieving successful motion correction when compared to the reference fixed LiDAR. Divergent cases (accounting for less than 0.5% of the statistical sample) were attributable to strong wind shears, which motivated retuning of the measurement-noise variance settings in Equation (38).

Figure 8 shows a low-turbulence case example, comparing a FDWL HWS measurement time-series with and without correction against the reference fixed-LiDAR time-series. Besides evident filter convergence, the motion-corrected HWS time-series matched almost ideally that of the reference LiDAR. The motion-induced error was greatly reduced from 0.14 m/s to 0.05 m/s RMSE, thus achieving good performance. When analyzing the PSD of these three time-series (see inset), it emerged that the RW model was able to emulate the wind process with high accuracy, up to some 21 dB roll-off at 7 Hz. However, the high-frequency components below −30 dB, which were not as relevant, were underestimated (data not shown).
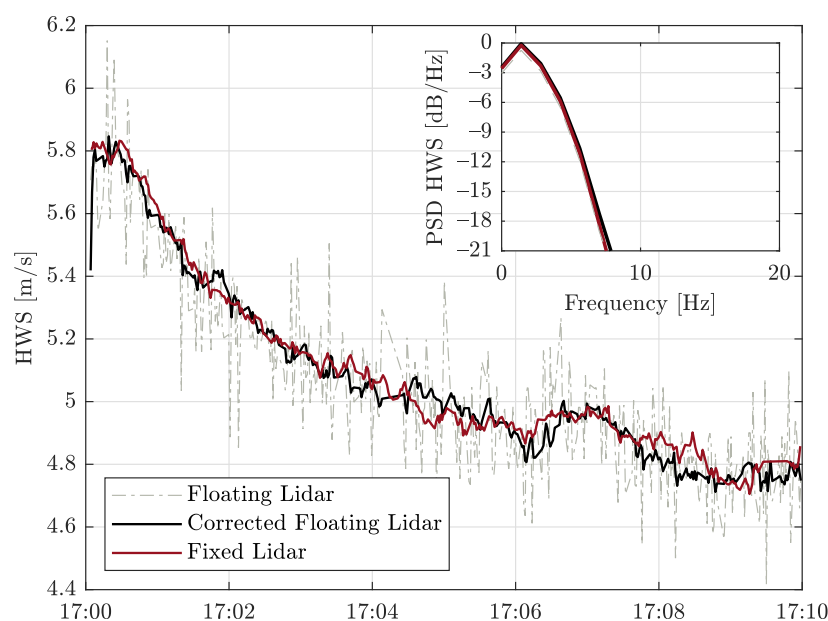
Figure 8. HWS time-series measured at 100 m height between the fixed LiDAR and the FDWL, with and without correction (see legend). Inset: PSD comparison. Low HWS-variance scenario (7 June 2013, PdP).

Underestimation of frequency components may lead to motion over-correction by the UKF in high variance scenarios, as illustrated in Figure 9. It can be observed that the motion-corrected FDWL and fixed-LiDAR temporal series only partially matched each other. Spectral analysis underlined differences between the HWS PSDs (red and black traces), being as high as 5 dB at low frequencies (0 to 5 Hz) and increasing to $\simeq$10 dB at high frequencies (5 to 20 Hz). This is a limitation of the used RW wind model, which was not able to emulate the high-frequency components of the wind spectrum. Consequently, the filter assimilated the wind model error as a measurement error, which led to biased estimations at specific times in Figure 9. Regarding 10-min WD estimation in either high-or low-variance scenarios (counterparts of Figures 8 and 9, respectively, data not shown), the filter was able to retrieve the yaw-error-free WD with a RMSE as low as roughly 5 deg for both the high- and low-variance cases. Regarding the so-called 1-s WD estimation, the "granularity" effect showed up in the retrieved time-series in similar fashion as for the retrieved HWS.
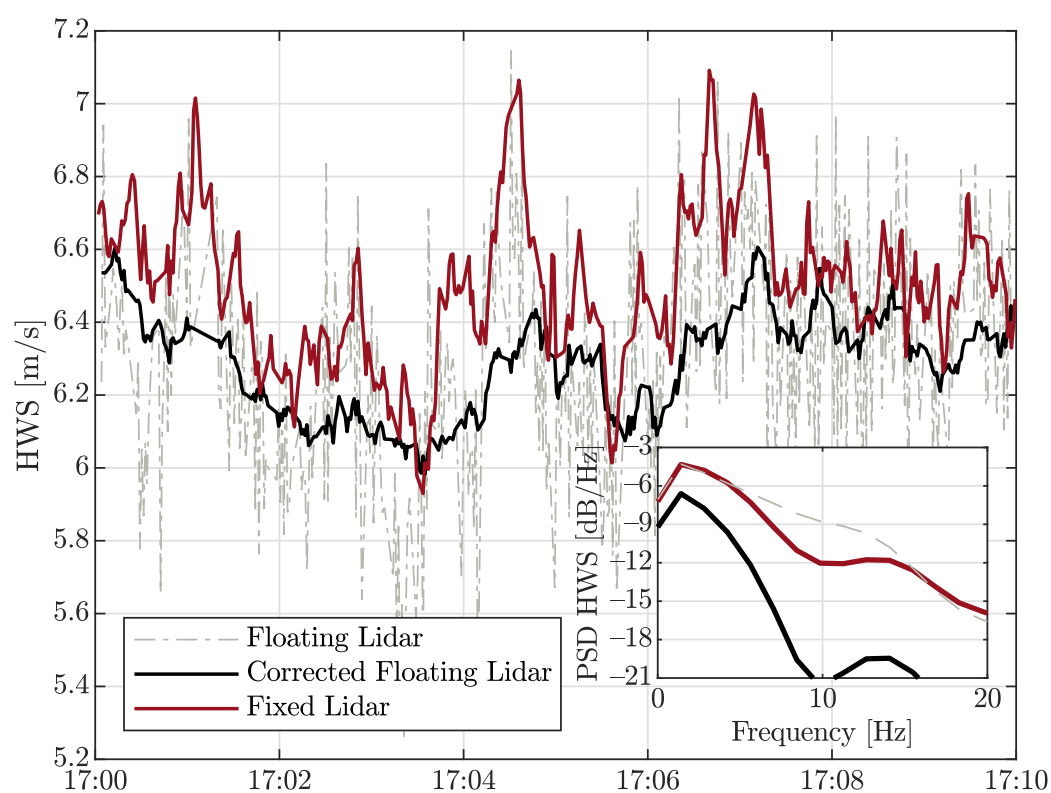
Figure 9. Same as Figure 8. High HWS-variance scenario (22 June 2013, PdP).

Overall campaign analysis.- With a view to assess the overall filter performance, the TIs measured by the FDWL during the PdP campaign (25 days, 1875 records) with and without correction ($TI_{float.,corr.}$ and $TI_{float.}$, respectively) were compared to the TI measured by the fixed LiDAR (TI_{fixed}). In the context of WE, the typical temporal resolution of wind-related data products is 10 min; thus, the comparison was carried out at 10 min temporal resolution. To carry out this comparison, different statistical indicators were considered: (i) The determination coefficient (R^2), (ii) RMSE, and (iii) mean deviation (MD).

The RMSE for a sample of N motion-corrected measurements is defined as

$$RMSE = \sqrt{\frac{\sum_n^N (TI_{float.,corr.} - TI_{fixed})^2}{N}}, \tag{40}$$

and the *MD* is defined as

$$MD = \frac{\sum_n^N TI_{float.,corr.} - TI_{fixed}}{N}. \tag{41}$$

The *MD* accounts for the systematic error in the LiDAR-measured *TI* (equivalently, HWS standard deviation) caused by wave-induced motion [9,46]. The RMSE and *MD* definitional formulae to compare FDWL uncorrected measurements to fixed-LiDAR measurements are analogous to Equations (40) and (41) above, by changing $TI_{float.,corr}$ to $TI_{float.}$.

The scatter plot shown in Figure 10 compares the *TI* measured by the FDWL (with and without correction) against the *TI* measured by the fixed LiDAR. Without correction, most of the $TI_{floating}$ values fell below the ideal 1:1 line. This was because buoy motion added an apparent variance to the HWS measurements, which increased the LiDAR-measured turbulence. The linear regression (LR, red dashed-dot line) offset of −0.0185 indicated the amount of added turbulence [14]. The LR slope of 1.0358, which is virtually identical to the ideal unity slope, indicates that the apparent turbulence equally affected all HWS measurements.
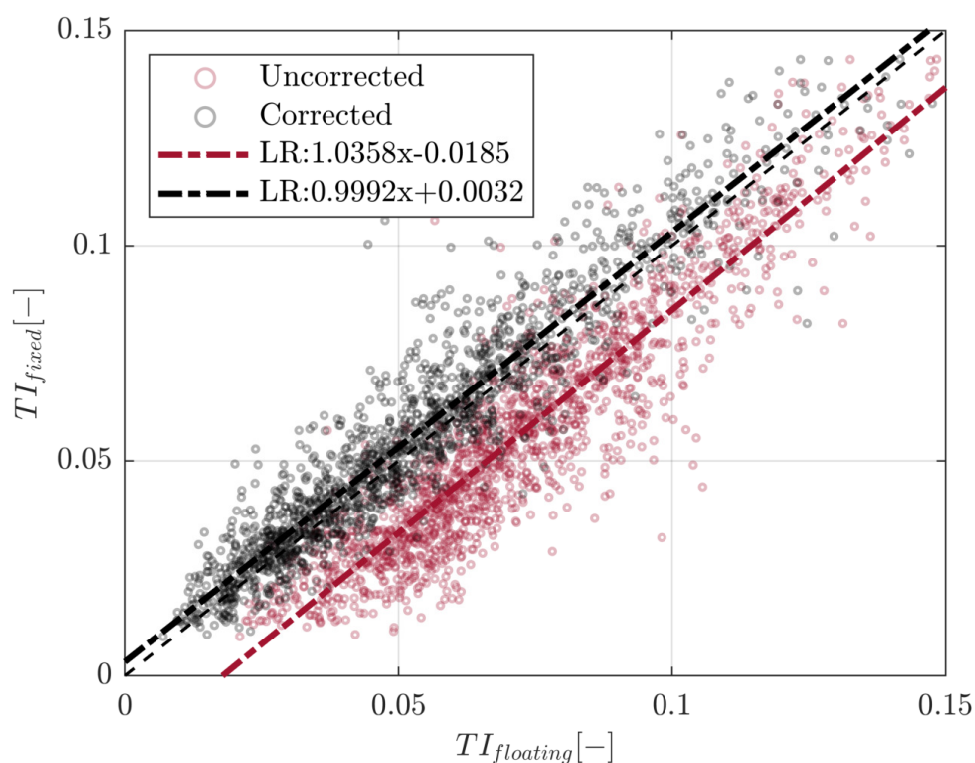
Figure 10. Scatter plot comparing the TI measured by the FDWL with reference to the fixed LiDAR, with and without correction (Red, without motion correction; Black, with motion correction). The dashed line indicates the ideal 1:1 line. Dot-dashed lines indicate corresponding color-coded linear regressions.

Regarding the motion-corrected TI measurements (black dots), the scatter points lay closer to the ideal 1:1 line, as demonstrated by an LR offset as low as 0.0032. This represented an 83% reduction factor, in comparison to the uncorrected measurements (offset term equal to 0.0185), and very small over-correction from the UKF side.

Scatter points away from the ideal 1:1 are a consequence of different filter model limitations: First, the LiDAR initial scan-phase model (Section 2.5.2) was unknown, the proposed RW models being only a reasonable rough approximation. Second, the retrieved WD by any of the two LiDAR instruments showed the so-called "granularity" issue, which

accounted for uncertainties of some ± 5 degrees (see Section 3.3), and which could have well led to inaccurate correction by the UKF. Finally, in Figure 10, we did not include the start-up period of the filter, in which the noise covariance matrices are still not well-estimated. Third, a more homogeneous terrain experimental scenario should be used. FDWLs are conceived for open-sea environments, and the motion-correction should be tested in these scenarios.

The overall campaign results demonstrated the good performance of the filter in reducing the apparent TI caused by buoy motion. All statistical indicators (see Table 1) improved: (i) the coefficient of determination, R^2, rose from 0.85 (without compensation) to 0.90 (with compensation); (ii) the RMSE reduced from 2.01% (without) to 1.01% (with); and (iii) the MD increased from −1.70% to 0.29%, accounting for an 83% factor improvement.

Table 1. Statistical indicators evaluating the comparison between FDWL (with and without correction) and fixed LiDAR TI measurements at the 10 min level.

	Uncorrected	Motion-Corrected	WD Filtered Motion-Corrected
R^2	0.85	0.90	0.93
RMSE	2.01%	1.01%	0.86%
MD	−1.70%	0.29%	0.36%

However, closer inspection of the measurement setup warrants some comments, regarding the statistical indicators shown: First, the floating and the fixed LiDARs were located 50 m apart and, although they measured similar wind conditions, the instantaneous wind measurements were not the same. This would have required setting up two LiDARs co-located at the same place. Specifically, winds blowing from/to the urban area (WDs between 270 and 330 deg, and between 90 and 150 deg, respectively) experienced higher spatial and temporal variation, due to terrain roughness [45], which led to different HWS time-series being measured by the LiDARs (see Section 3.3).

According to Taylor's frozen-atmosphere theory [47], turbulent eddies transported by the mean wind hold their properties as if they were "frozen", such that two points aligned with the mean WD will observe the same wind stochastic realization, with a time delay. This delay is inversely proportional to the mean HWS. The floating and the fixed LiDARs were mainly aligned along the north-south direction and, therefore, only measurement records with WDs within 180±30 deg will be considered for further, enhanced statistical analysis. The maximum delay measured between the two LiDARs was 25 s, which is a negligible value, compared to the measurement period of 10 min.

After the WD was filtered, as indicated, the statistical indicators improved, as shown in the third column of Table 1. The coefficient of determination increased to 0.93 and the RMSE decreased to 0.86%. The small increase in MD (0.36%) was not significant, on account of the approximate WD filtering procedure.

4. Conclusions

An adaptive method for 6-DoF motion compensation of ZephIR 300 FDWL wind measurements was presented in this paper. The RAUKF algorithm proved to be capable of correcting the motion-induced error in the retrieved HWS (Figure 8) and TI (Figure 10), without accessing LiDAR LoS velocity measurements, which is undisclosed information from the manufacturer's side for most of the commercial continuous-wave wind LiDARs. To the best of our knowledge, this is a key state-of-the-art contribution of this work.

The proposed solution departed from the FDWL motion dynamics study [20] and the well-known VAD wind-retrieval algorithm, to derive an ad-hoc state-space formulation of the problem from the point of view of control theory, using an UKF and stochastic modelling. The state-vector transition model relied on a RW model to describe the unknown motion-corrected wind vector (to be found) and blind LiDAR initial scan phase. The measurement model was time variant and combined the buoy's 6-DoF IMU information with

the filter's estimated motion-corrected wind vector, to predict the FDWL motion-corrupted wind measurements. The recursive loop of the filter, combined with run-time estimation of the state-vector and measurement-noise covariance matrices, ensured successful and convergent results.

The methodology was validated using the experimental data collected during a PdP measurement campaign in Barcelona, using a fixed LiDAR on the PdP pier as the reference instrument. To quantitatively assess filter performance, the 10 min TI measured by the FDWL with and without correction was compared to the TI measured by the reference LiDAR. Wind measurements were also WD screened, to ensure the validity of Taylor's frozen-atmosphere assumption along the connecting line between the two LiDARs. All statistical indicators showed significant improvement Table 1: MD improved from −1.60% (without correction) to 0.36% (with correction), the RMSE improved from 1.9% to 0.86%, and the determination coefficient (R^2) increased from 0.86 to 0.93. Linear regression between floating- and fixed-TI measurements showed an offset equal to the apparent motion-induced TI added; which, upon correction by the filter, was virtually removed.

A limitation of the filter was its underestimation of the high-frequency components (i.e., fast transients) when comparing floating-lidar HWS temporal series with reference to fixed-LiDAR ones. This was due to the oversimplified RW wind model used. Notwithstanding the overall improvement in all the statistical indicators shown, a few outliers departed from the ideal 1:1 line between the motion-corrected and fixed-LiDAR TI observations. We hypothesize that this may be due to the filter start-up time (about 60 s before stable tracking condition is reached), as well as the so-called "granularity" effect in the LiDAR-retrieved WD.

All in all, the RAUKF was demonstrated to be an effective tool for 6-DoF motion correction of FDWL measurements and accurate TI measurements. Furthermore, the recursive operation of the filter allows room for stand-alone, nearly real-time correction of FDWL measurements.

Abbreviations

The following abbreviations are used in this manuscript:

DoF	Degrees of Freedom
DWL	Doppler Wind LiDAR
EKF	Extended Kalman Filter
FDWL	Floating Doppler Wind LiDAR
HWS	Horizontal Wind Speed
IMU	Inertial Measurement Unit
KF	Kalman Filter
LoS	Line-of-Sight
LSQ	Least Squares
MD	Mean Deviation
metmast	meteorological mast
PdP	El Pont del Petroli
PSD	Power Spectral Density
RAUKF	Robust Adaptive Unscented Kalman Filter
RMSE	Root Mean Square Error
RW	Random Walk
SV	Spatial Variation
TI	Turbulence Intensity
UKF	Unscented Kalman Filter
VAD	Velocity–Azimuth Display
VWS	Vertical Wind Speed
WD	Wind Direction
WE	Wind Energy

Appendix A. Kalman Filter Review

This Section summarizes the study on UKF by Wan et al. [48], for self-completeness of the theoretical foundations given in Section 2.3. The reader is referred to this reference for further insight.

The Kalman Filter (KF) is a recursive filter that optimally estimates the internal (i.e., hidden) state-vector of a linear dynamic system from noisy observations, as described in Section 2.3. The KF is the optimal estimator for linear systems under a statistical minimum-variance criterion over time. In contrast, the Extended Kalman Filter (EKF) is one of the most widely used methods to estimate the state variables of non-linear systems, as is the case of moving FDWLs. The main limitation of the EKF is that it linearizes system non-linearities by first-order Taylor's series expansion. This implies propagation of the random variables distribution (RVD) through the system equations, which usually leads to large errors in the statistical moments of the transformed variables and, hence, to sub-optimal filter performance. The Unscented Kalman Filter (UKF) provides an elegant solution to solve these weaknesses [48].

Appendix A.1. The Unscented Transform

The UKF addresses the RVD approximation errors of the EKF by means of the unscented transform (UT). In the UT, a set of samples representative of the mean and covariance of the RVD are chosen. These samples are propagated through the non-linear dynamics of the system, to accurately capture the system-propagated RVD mean and covariance. This is formulated in the following:

Consider an N-dimensional random variable $\boldsymbol{x}$ (e.g., the state-vector previously introduced in Section 2.3) with mean $\bar{\boldsymbol{x}}$ and covariance $\boldsymbol{P_x}$ propagating through a non-linear function $f(\cdot)$ (e.g., the state-transition function of Section 2.3), $\boldsymbol{y} = f(\boldsymbol{x})$. The UT chooses a set of $2N + 1$ auxiliary vectors (the so-called *sigma vectors*), $\boldsymbol{\chi_i}$, to estimate the RVD [49].

Their sample mean and sample covariance are $\bar{x}$ and P_x, respectively. The *sigma vectors* are chosen as

$$\chi_0 = \bar{x} \tag{A1}$$

$$\chi_i = \bar{x} + (\sqrt{(L+\lambda)P^{xx}})_i \qquad i = 1,\ldots,L \tag{A2}$$

$$\chi_i = \bar{x} - (\sqrt{(L+\lambda)P^{xx}})_i \qquad i = L+1,\ldots,2L, \tag{A3}$$

where $(\sqrt{(L+\lambda)P^{xx}})_i$ denotes the ith row of the square-root matrix, and λ is a scaling parameter (typically, $\lambda = 3 - N$ for Gaussian distributions). When *sigma* vectors χ propagate through the non-linear function $f(x)$, a transformed variable set, v_i, is obtained,

$$v_i = f(\chi^i). \tag{A4}$$

The sought-after mean and covariance of system output variable y are approximated as a weighted mean of the propagated sigma points,

$$\bar{y} \simeq \sum_{i=0}^{2N} W_i^m v^i, \tag{A5}$$

$$P^{yy} \simeq \sum_{i=0}^{2N} W_i^m (v^i - \bar{y})(v^i - \bar{y})^T, \tag{A6}$$

where the weights are defined as

$$W_0^m = W_0^c = \lambda/(N+\lambda), \tag{A7}$$
$$W_i^m = W_i^c = 1/(2(N+\lambda)). \tag{A8}$$

Appendix A.2. The Unscented Kalman Filter

The UKF uses the UT to estimate the RVDs of both the state-vector and the observation vector. The recursive algorithm of the filter can be summarized by the following ten-step procedure:

Step 1. Initialize the filter with the initial-guess state-vector and state-vector covariance, as:

$$\hat{x}_0 = E[x_k^T] \tag{A9}$$
$$\hat{P}_0^{xx} = E[(x_0 - \hat{x}_0)(x_0 - \hat{x}_0)^T]. \tag{A10}$$

Step 2. Calculate the sigma points at discrete time $k-1$, used as a proxy of the state-vector RVD (see Appendix A.1), as:

$$\chi_{k-1} = \left[\hat{x}_{k-1} \quad x_{k-1} \pm \sqrt{(L + \hat{P}_{k-1|k-1}^{xx})}\right]. \tag{A11}$$

Step 3. Compute the sigma-points output at time k, in response to the sigma points input at time $k-1$, by the system state-transition function, $f(\cdot)$, as:

$$\chi_{k|k-1} = f(\chi_{k-1}). \tag{A12}$$

Step 4. Obtain the predicted *a priori* state-vector mean and covariance matrix at time k, as:

$$\bar{x}_{k|k-1} = \sum_{i=0}^{2N} W_i^m \chi_{k|k-1}^i \tag{A13}$$

$$P_{k|k-1}^{xx} = \sum_{i=0}^{2N} W_i^c [\chi_{k|k-1}^i - \bar{x}_{k|k-1}][\chi_{k|k-1}^i - \bar{x}_{k|k-1}]^T + Q_k, \tag{A14}$$

where Q_k is the state-noise covariance matrix defined in Section 2.7.

Step 5. Propagate the sigma-points set computed in Step 3 above, through the nonlinear measurement function $h(\cdot)$, to obtain the so-called *sigma-Z* points, as:

$$Z_{k|k-1} = h(\chi_{k|k-1}). \tag{A15}$$

Step 6. Estimate the mean and covariance of the *innovation* set at time k from the obtained sigma-Z points and observation-noise covariance matrix, R_k (refer to Section 2.7),

$$\bar{z}_{k|k-1} = \sum_{i=0}^{2N} W_i^m Z_{k|k-1}^i. \tag{A16}$$

$$P_{k|k-1}^{zz} = \sum_{i=0}^{2N} W_i^c [Z_{k|k-1}^i - \bar{z}_{k|k-1}][Z_{k|k-1}^i - \bar{z}_{k|k-1}]^T + R_k. \tag{A17}$$

In Equation (A17) above, Z denotes the sigma-Z points in the UT domain, whereas z denotes the observation vector in the "non-transformed" measurement domain (e.g., the LiDAR wind-vector measurements). An overbar is used to indicate the approximated mean, by means of the UT as computed in Appendix A.1.

Step 7. Compute the *a priori* state-vector covariance matrix at time k, as the cross covariance between $\bar{x}_{k|k-1}$ and $\bar{z}_{k|k-1}$:

$$P_{k|k-1}^{xz} = \sum_{i=0}^{2N} W_i^c [\chi_{k|k-1}^i - \bar{x}_{k|k-1}][Z_{k|k-1}^i - \bar{z}_{k|k-1}]^T. \tag{A18}$$

Step 8. Derive the Kalman gain as

$$K_k = P_{k|k-1}^{xz}(P_{k|k-1}^{zz})^{-1}. \tag{A19}$$

Step 9. Compute the *a posteriori* state-vector and *a posteriori* covariance as:

$$\hat{x}_k = \bar{x}_{k|k-1} + K_k(z_k - \bar{z}_{k|k-1}) \tag{A20}$$

$$\hat{P}_{k|k}^{xx} = P_{k|k-1}^{xx} - P_{k|k-1}^{zz} - K_k P_{k|k-1}^{zz} K^T. \tag{A21}$$

Step 10. (Recursive step) Time update and go to Step 2:

$$\hat{x}_{k-1} = \hat{x}_k \tag{A22}$$

$$\hat{P}_{k-1|k-1}^{xx} = \hat{P}_{k|k}^{xx}. \tag{A23}$$

Appendix B. RAUKF Fault-Detection Mechanism

The RAUKF algorithm uses the fault-detection mechanism described in the study by Zheng et al. [34]. In short, this method computes a test variable ϕ_k, which signals the need to re-adjust the covariance matrices R_k and Q_k. The test variable at time k is defined as

$$\phi_k = [z_k - h(\bar{x}_{k|k-1})]^T [P_{k|k-1}^{zz}]^{-1} [z_k - h(\bar{x}_{k|k-1})]. \tag{A24}$$

ϕ_k follows a χ^2 distribution with s DoFs, where s is the dimension of vector $\boldsymbol{\mu}_k = \boldsymbol{z}_k - h(\overline{x}_{k|k-1})$ ($s = 3$ in the case of Equation (1) wind vector). To detect a fault with reliability $1 - \sigma$ (where σ is a preset value), a threshold $\chi^2_{s,\sigma}$ is set, such that

$$P(\phi_k > \chi^2_{s,\sigma}) = \sigma. \tag{A25}$$

With these settings, a fault is detected with reliability $1 - \sigma$ when $\phi_k > \chi^2_{s,\sigma}$, which means that covariance matrices $\boldsymbol{R}$ and $\boldsymbol{Q}$ must be re-adjusted. $\chi^2_{s,\sigma}$ defines the error detection reliability (e.g., for 90% reliability, set $\sigma = 0.1$). If $s = 3$ DoF (as is the case here) then $\chi^2_{3,0.1}$ must be set to 6.36. The variables σ and $\chi^2_{s,\sigma}$ indicate the confidence we have in the system model and the related noise covariance matrices. Thus, the higher the threshold $\chi^2_{s,\sigma}$, the lower the probability that an error is interpreted as a model fault.

References

1. Global Wind Energy Council. *Global Wind Report 2018*; Technical Report; Global Wind Energy Council: Brussels, Belgium, 2019.
2. Barthelmie, R.; Courtney, M.; Højstrup, J.; Larsen, S. Meteorological aspects of offshore wind energy: Observations from the Vindeby wind farm. *J. Wind. Eng. Ind. Aerodyn.* **1996**, *62*, 191–211. [CrossRef]
3. *Offshore Wind in Europe Key Trends and Statistics 2019*; Technical Report; WindEurope: Brussels, Belgium, 2020.
4. Timmons, D. 25 - Optimal Renewable Energy Systems: Minimizing the Cost of Intermittent Sources and Energy Storage. In *A Comprehensive Guide to Solar Energy Systems*; Letcher, T.M., Fthenakis, V.M., Eds.; Academic Press: Cambridge, MA, USA, 2018; pp. 485–504. [CrossRef]
5. Carbon Trust. *Carbon Trust Offshore Wind Accelerator Roadmap for the Commercial Acceptance of Floating LIDAR Technology*; Technical Report; Carbon Trust: London, UK, 2013.
6. Peña, A.; Hasager, C.; Lange, J.; Anger, J.; Badger, M.; Bingöl, F.; Bischoff, O.; Cariou, J.P.; Dunne, F.; Emeis, S.; et al. *Remote Sensing for Wind Energy*; DTU Wind Energy: Roskilde, Denmark, 2013.
7. Sathe, A.; Mann, J. A review of turbulence measurements using ground-based wind lidars. *Atmos. Meas. Tech.* **2013**, *6*, 3147–3167. [CrossRef]
8. Berger, R. *Offshore Wind toward 2020: On the Pathway to Cost Competitiveness*; Technical Report; Roland Berger: Munich, Germany, 2013.
9. Gutiérrez, M.A.; Tiana-Alsina, J.; Bischoff, O.; Cateura, J.; Rocadenbosch, F. Performance evaluation of a floating Doppler wind lidar buoy in mediterranean near-shore conditions. In Proceedings of the 2015 IEEE International Geoscience and Remote Sensing Symposium (IGARSS), Milan, Italy, 26–31 July 2015; pp. 2147–2150. [CrossRef]
10. Gutierrez-Antunano, M.A.; Tiana-Alsina, J.; Rocadenbosch, F.; Sospedra, J.; Aghabi, R.; Gonzalez-Marco, D. A wind-lidar buoy for offshore wind measurements: First commissioning test-phase results. In Proceedings of the 2017 IEEE International Geoscience and Remote Sensing Symposium (IGARSS-2017), Fort Worth, TX, USA, 23–28 July 2017; IEEE: Fort Worth, TX, USA, 2017; pp. 1607–1610. [CrossRef]
11. Schuon, F.; González, D.; Rocadenbosch, F.; Bischoff, O.; Jané, R. KIC InnoEnergy Project Neptune: Development of a Floating LiDAR Buoy for Wind, Wave and Current Measurements. In Proceedings of the DEWEK 2012 German Wind Energy Conference, Bremen, Germany, 19–20 May 2012.
12. Mathisen, J.P. Measurement of wind profile with a buoy mounted lidar. *Energy Procedia* **2013**, *30*, 12.
13. Gutiérrez-Antuñano, M.; Tiana-Alsina, J.; Salcedo, A.; Rocadenbosch, F. Estimation of the Motion-Induced Horizontal-Wind-Speed Standard Deviation in an Offshore Doppler Lidar. *Remote Sens.* **2018**, *10*, 2037. [CrossRef]
14. Salcedo-Bosch, A.; Gutierrez-Antunano, M.A.; Tiana-Alsina, J.; Rocadenbosch, F. Floating Doppler Wind Lidar Measurement of Wind Turbulence: A Cluster Analysis. In Proceedings of the 2020 IEEE International Geoscience and Remote Sensing Symposium (IGARSS-2020), Waikoloa, HI, USA, 26 September–2 October 2020.
15. Courtney, M.S.; Hasager, C.B. Remote sensing technologies for measuring offshore wind. In *Offshore Wind Farms*; Elsevier: Amsterdam, The Netherlands, 2016; Chapter 4, pp. 59–82.
16. Mücke, T.; Kleinhans, D.; Peinke, J. Atmospheric turbulence and its influence on the alternating loads on wind turbines. *Wind Energy* **2011**, *14*, 301–316. [CrossRef]
17. Gottschall, J.; Gribben, B.; Stein, D.; Würth, I. Floating lidar as an advanced offshore wind speed measurement technique: Current technology status and gap analysis in regard to full maturity. *Wiley Interdiscip. Rev. Energy Environ.* **2017**, *6*, e250. [CrossRef]
18. Gottschall, J.; Wolken-Möhlmann, G.; Lange, B. About offshore resource assessment with floating lidars with special respect to turbulence and extreme events. *J. Phys. Conf. Ser.* **2014**, *555*, 12–43. [CrossRef]
19. Tiana-Alsina, J.; Rocadenbosch, F.; Gutierrez-Antunano, M.A. Vertical Azimuth Display simulator for wind-Doppler lidar error assessment. In Proceedings of the 2017 IEEE International Geoscience and Remote Sensing Symposium (IGARSS), Fort Worth, TX, USA, 23–28 July 2017; pp. 1614–1617. [CrossRef]
20. Kelberlau, F.; Neshaug, V.; Lønseth, L.; Bracchi, T.; Mann, J. Taking the Motion out of Floating Lidar: Turbulence Intensity Estimates with a Continuous-Wave Wind Lidar. *Remote Sens.* **2020**, *12*, 898. [CrossRef]

21. Gutiérrez-Antuñano, M.A.; Tiana-Alsina, J.; Rocadenbosch, F. Performance evaluation of a floating lidar buoy in nearshore conditions. *Wind Energy* **2017**, *20*, 1711–1726. [CrossRef]
22. Mann, J. Wind field simulation. *Probabilistic Eng. Mech.* **1998**, *13*, 269–282. [CrossRef]
23. Brown, B.G.; Katz, R.W.; Murphy, A.H. Time series models to simulate and forecast wind speed and wind power. *J. Appl. Meteorol. Climatol.* **1984**, *23*, 1184–1195. [CrossRef]
24. Rodgers, C.D. *Inverse Methods for Atmospheric Sounding: Theory and Practice*; Series on Atmospheric, Oceanic and Planetary Physics; World Scientific: Singapore, 2004; Volume 2.
25. Robert Grover, R.; Hwang, P.Y.C. *Introduction to Random Signals and Kalman Filtering: With MATLAB Exercises*, 4th ed.; Wiley: Hoboken, NJ, USA, 2012.
26. Slinger, C.; Harris, M. Introduction to Continuous-Wave Doppler Lidar. Available online: http://breeze.colorado.edu/ftp/RSWE/Chris_Slinger.pdf (accessed on 21 July 2021)
27. Sospedra, J.; Cateura, J.; Puigdefàbregas, J. Novel multipurpose buoy for offshore wind profile measurements EOLOS platform faces validation at ijmuiden offshore metmast. *Sea Technol.* **2015**, *56*, 25–28.
28. ZX Lidars. *ZX 300M—Offshore Wind Measurements from Vertical Profiling Lidar*; ZX Lidars: Ledbury, UK, 2021.
29. Pitter, M.; Burin des Roziers, E.; Medley, J.; Mangat, M.; Slinger, C.; Harris, M. *Performance Stability of Zephir in High Motion Enviroments: Floating and Turbine Mounted*; Technical Report; ZephIR: Ledbury, UK, 2014.
30. Smith, D.A.; Mehta, K.C. Investigation of stationary and nonstationary wind data using classical Box-Jenkins models. *J. Wind. Eng. Ind. Aerodyn.* **1993**, *49*, 319–328. [CrossRef]
31. Davari, N.; Gholami, A. An Asynchronous Adaptive Direct Kalman Filter Algorithm to Improve Underwater Navigation System Performance. *IEEE Sens. J.* **2017**, *17*, 1061–1068. [CrossRef]
32. Koivisto, M.; Seppänen, J.; Mellin, I.; Ekström, J.; Millar, J.; Mammarella, I.; Komppula, M.; Lehtonen, M. Wind speed modeling using a vector autoregressive process with a time-dependent intercept term. *Int. J. Electr. Power Energy Syst.* **2016**, *77*, 91–99. [CrossRef]
33. Li, W.; Sun, S.; Jia, Y.; Du, J. Robust unscented Kalman filter with adaptation of process and measurement noise covariances. *Digit. Signal Process.* **2016**, *48*, 93–103. [CrossRef]
34. Zheng, B.; Fu, P.; Li, B.; Yuan, X. A Robust Adaptive Unscented Kalman Filter for Nonlinear Estimation with Uncertain Noise Covariance. *Sensors* **2018**, *18*, 808. [CrossRef]
35. Wang, J. Stochastic Modeling for Real-Time Kinematic GPS/GLONASS Positioning. *Navigation* **1999**, *46*, 297–305. [CrossRef]
36. Hajiyev, C.; Soken, H.E. Robust adaptive unscented Kalman filter for attitude estimation of pico satellites. *Int. J. Adapt. Control. Signal Process.* **2014**, *28*, 107–120. [CrossRef]
37. Lange, D.; Rocadenbosch, F.; Tiana-Alsina, J.; Frasier, S. Atmospheric Boundary Layer Height Estimation Using a Kalman Filter and a Frequency-Modulated Continuous-Wave Radar. *IEEE Trans. Geosci. Remote Sens.* **2015**, *53*, 3338–3349. [CrossRef]
38. Salcedo-Bosch, A.; Rocadenbosch, F.; Gutiérrez-Antuñano, M.A.; Tiana-Alsina, J. Estimation of Wave Period from Pitch and Roll of a Lidar Buoy. *Sensors* **2021**, *21*, 1310. [CrossRef]
39. Salcedo-Bosch, A.; Gutierrez-Antunano, M.A.; Tiana-Alsina, J.; Rocadenbosch, F. Motional Behavior Estimation Using Simple Spectral Estimation: Application to the Off-Shore Wind Lidar. In Proceedings of the 2020 IEEE International Geoscience and Remote Sensing Symposium (IGARSS-2020), Waikoloa, HI, USA, 26 September–2 October 2020.
40. National Data Buoy Center. *Nondirectional and Directional Wave Data Analysis Procedures*; Technical Report; National Oceanic and Atmospheric Administration: Washington, DC, USA, 1996.
41. Wagner, R.; Mikkelsen, T.; Courtney, M. *Investigation of Turbulence Measurements with a Continuous Wave, Conically Scanning LiDAR*; Technical Report; DTU: Roskilde, Denmark, 2009.
42. Gutiérrez Antuñano, M.Á. Doppler Wind LIDAR Systems Data Processing and Applications: An Overview towards Developing the New Generation of Wind Remote-Sensing Sensors for Off-Shore Wind Farms. Ph.D. Thesis, Polytechnic University of Catalonia, Barcelona, Spain, 2019.
43. Campbell Scientific. *ZephIR 300*; Technical Report; Campbell Scientific: Edmonton, AB, Canada, 2016.
44. Bingöl, F.; Mann, J.; Foussekis, D. Conically scanning lidar error in complex terrain. *Meteorol. Z.* **2009**, *18*, 189–195. [CrossRef]
45. Al-Khalidy, N. Building Generated Wind Shear and Turbulence Prediction Utilising Computational Fluid Dynamics. *WSEAS Trans. Fluid Mech.* **2018**, *13*, 126–135.
46. Gottschall, J.; Wolken-Möhlmann, G.; Viergutz, T.; Lange, B. Results and conclusions of a floating-lidar offshore test. *Energy Procedia* **2014**, *53*, 156–161. [CrossRef]
47. Taylor, G.I. The spectrum of turbulence. *Proc. R. Soc. Lond. Ser. A Math. Phys. Sci.* **1938**, *164*, 476–490. [CrossRef]
48. Wan, E.A.; Van Der Merwe, R. The unscented Kalman filter for nonlinear estimation. In Proceedings of the IEEE 2000 Adaptive Systems for Signal Processing, Communications, and Control Symposium (Cat. No.00EX373), Lake Louise, AB, Canada, 4 October 2000; pp. 153–158. [CrossRef]
49. Julier, S.J.; Uhlmann, J.K. New extension of the Kalman filter to nonlinear systems. In *Signal Processing, Sensor Fusion, and Target Recognition VI*; Kadar, I., Ed.; International Society for Optics and Photonics, SPIE: Bellingham, WA, USA, 1997; Volume 3068, pp. 182–193. [CrossRef]